



## Generation of magnetic skyrmions in two-dimensional magnets via interfacial proximity

Yun Zhang <sup>1,\*</sup>,† Huisheng Zhang,<sup>2,\*</sup> Jingman Pang,<sup>3</sup> Yue Ma,<sup>1</sup> Meiguang Zhang <sup>1</sup>, Xiaohong Xu,<sup>2</sup> and Laurent Bellaïche<sup>4,‡</sup>

<sup>1</sup>College of Physics and Optoelectronic Technology, Collaborative Innovation Center of Rare-Earth Functional Materials and Devices Development, Baoji University of Arts and Sciences, Baoji 721016, China

<sup>2</sup>Key Laboratory of Magnetic Molecules and Magnetic Information Materials of Ministry of Education & Research Institute of Materials Science, Shanxi Normal University, Taiyuan 030006, China

<sup>3</sup>Department of Materials Science and Engineering, Xi'an University of Technology, Xi'an, Shaanxi 710048, People's Republic of China

<sup>4</sup>Physics Department and Institute for Nanoscience and Engineering, University of Arkansas, Fayetteville, Arkansas 72701, USA



(Received 6 July 2022; revised 15 November 2022; accepted 15 December 2022; published 3 January 2023)

Two-dimensional (2D) magnetic van der Waals materials provide a fertile platform for the design and control of topological spin textures such as skyrmions. However, despite studies reporting skyrmions in many 2D magnetic systems, the hosting van der Waals materials are still limited. Here, via first-principles calculations and Monte Carlo simulations, we propose a series of 2D magnetic heterostructures as a different materials' family hosting skyrmions. Unlike previously studied van der Waals heterostructures, a strong interface coupling generates here a significant inversion symmetry breaking, which then results in an inherently large Dzyaloshinskii-Moriya interaction (DMI). Furthermore, upon applying a moderate magnetic field, isolated skyrmions and skyrmions lattices emerge in various types of these heterostructures, and are robust within a relatively wide temperature range. Our work thus suggests a general method to induce DMI and paves the way toward topological magnetism in 2D materials through interfacial engineering.

DOI: [10.1103/PhysRevB.107.024402](https://doi.org/10.1103/PhysRevB.107.024402)

### I. INTRODUCTION

Magnetic skyrmions, which are topologically protected spin textures, have recently attracted rising attention for their potential applications to the next-generation information storage and processing device, such as racetrack memory [1–4]. One typical requirement towards the formation of skyrmions is the antisymmetric exchange interaction, known as Dzyaloshinskii-Moriya interaction (DMI), which originates from the spin-orbit coupling (SOC). DMI only exists in systems having no local inversion symmetry [5,6], such as single crystals [1,7–10] and several thin-film systems [11–15]. The latter one as well as the magnetic multilayered systems with asymmetric interfaces have gained great interest as a skyrmion host, due to their natural inversion symmetry breaking and tunable magnetic parameters by varying the thickness of the layers and the composition at the interface.

Furthermore, the recent discovery of long-range magnetic order in two-dimensional (2D) materials, represented by CrI<sub>3</sub> and CrGeTe<sub>3</sub>/CrSiTe<sub>3</sub>, provides a promising platform for exploring exotic magnetic phenomena down to the 2D limit [16–19]. Due to the large SOC of the ligand atom I/Te, these compounds exhibit sizable magnetic anisotropy energy (MAE), which is responsible for the long-range 2D magnetism. One may now wonder if pronounced DMI can be induced in these 2D magnets once the inversion symmetry is broken. Recent reports have demonstrated several strategies to break inversion symmetry of 2D magnets: Janus structures

[20–24], perpendicular electric field [25], and heterostructures [26–31]. Among these, like the magnetic multilayered systems, 2D van der Waals (vdW) magnetic heterostructures with intrinsic inversion asymmetry have received particular attention. For example, bimerons have been discovered in the LaCl/In<sub>2</sub>Se<sub>3</sub> heterostructure and can be manipulated by ferroelectric polarization in In<sub>2</sub>Se<sub>3</sub> [27]. Li *et al.* have also shown the existence of the skyrmion in a Cr<sub>2</sub>Ge<sub>2</sub>Te<sub>6</sub>/In<sub>2</sub>Se<sub>3</sub> heterostructure [29]. However, the interfacial induced DMI is relatively small ( $|D/J|$  is 0.05 for WTe<sub>2</sub>/CrCl<sub>3</sub> [28], 0.04 for Cr<sub>2</sub>Ge<sub>2</sub>Te<sub>6</sub>/In<sub>2</sub>Se<sub>3</sub> [29], 0.055 for CrTe<sub>2</sub>/WTe<sub>2</sub> [30], and 0.045 for strained Fe<sub>3</sub>GeTe<sub>2</sub>/germanene [31]) in the weak vdW heterostructures, which is out of the typical  $|D/J|$  range 0.1–0.2 known to generate skyrmionic phases as ground state [32]. Thus, a strong interfacial interaction in 2D magnetic heterostructures is highly desired to obtain a large interfacial DMI. Here, we propose a general effective way to induce large DMI in 2D magnets via strong interfacial coupling in a series of heterostructures that consist of a ferromagnetic (FM) CrXTe<sub>3</sub> monolayer ( $X = \text{Si, Ge, and Sn}$ ) and a buckled  $Y$  ( $Y = \text{germanene and silicene}$ ) monolayer, as shown in Fig. 1. As we will show, due to strong interfacial interaction, these  $Y$ -CrXTe<sub>3</sub> heterostructures do exhibit large DMIs. Moreover, upon applying a moderate magnetic field, isolated skyrmions and skyrmions lattices can be obtained in several of these heterostructures, which is revealed to be robust within a relatively wide temperature range. Our results therefore provide an efficient strategy to induce large DMI in 2D magnets via strong interfacial coupling other than constructing typical vdW heterostructures. Such a strategy should be helpful to design novel 2D skyrmion-based logic and memory devices.

\*These authors contributed equally to this work.

†zhangyun\_xtu@163.com

‡laurent@uark.edu

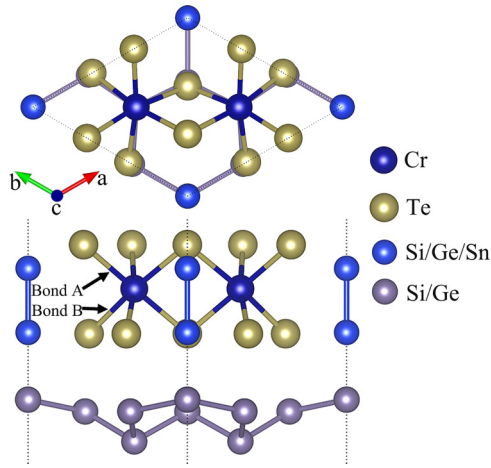


FIG. 1. Top and side views of  $Y\text{-CrXTe}_3$  heterostructures. Bonds A and B denote the Cr-Te bond close to and away from the interface, respectively.

The rest of the paper is organized as follows. In Sec. II, we describe the computational methods presently employed. In Sec. III, we report and discuss our results, including the structural model used in the calculations (Sec. III A); the magnetic exchange parameters for all heterostructures, with a particular emphasis on the impact of the interface coupling on the DMI (Sec. III B); the extracted magnetic parameters, Curie temperatures, and ground states determined via Monte Carlo (MC) simulations (Sec. III C); the effects of magnetic field on topological spin textures (Sec. III D); and the magnetic field-versus-temperature phase diagram ( $B$ - $T$ ), as well as a discussion about thermal fluctuation effects on topology (Sec. III E). Section IV briefly summarizes our work.

## II. COMPUTATIONAL METHODS

We have performed first-principles calculations based on the density-functional theory (DFT) implemented in the Vienna ab initio simulation package (VASP) [33,34]. The energy cutoff for the plane wave basis expansion is set to be 350 eV. A 15-Å layer is used to avoid interaction between adjacent layers. The Perdew-Burke-Ernzerhof (PBE) approximation was used to describe the exchange and correlation functional [35]. To better describe the Cr  $3d$  electrons, the generalized gradient approximation (GGA) +  $U$  method is employed, in which an effective Hubbard  $U_{\text{eff}}$  is set to 3.0 eV. We also calculated the difference in energy between ferromagnetic and antiferromagnetic states,  $\Delta E = E_{\text{fm}} - E_{\text{afm}}$ , of the eight heterostructures indicated in Table S1 of the Supplemental Material [43], by varying  $U_{\text{eff}}$ . As indicated in this Table S1, we find that the ferromagnetism in all heterostructures is robust to  $U_{\text{eff}}$  values. Therefore, we choose a moderate value of  $U = 3.0$  eV. The  $12 \times 12 \times 1$  gamma-centered  $k$ -point mesh was used to sample the Brillouin zone of the unit cell for structural optimization and  $30 \times 30 \times 1$   $k$ -point mesh was employed for calculating the magnetic anisotropic energy and the energy difference between the ferromagnetic and antiferromagnetic states. The vdW correction with the Grimme (DFT-D2) method is included in the structural calculations [36]. For geometry optimization, all the internal coordinates

are fully relaxed until the Hellmann-Feynman forces on each atom are less than 0.01 eV/Å. The four-state energy mapping method is applied to obtain the symmetric exchange parameter ( $J$ ) and the antisymmetric DM interaction parameter ( $D$ ) [37]. To ensure accuracy, we choose a  $3 \times 3 \times 1$  supercell for the four-state method calculations, which is proven to be large enough to prevent the coupling between some sites present in the supercell and periodically repeated sites [38]. See Refs. [39,40] for more details.

Based on calculated magnetic parameters, the parallel tempering Monte Carlo (MC) simulations are carried out to explore the spin textures and estimate Curie temperature ( $T_C$ ) with the Material Simulation and Property Calculation Package (MSPCP) [41,42]. The details of MC simulations are given in the Supplemental Material [43].

## III. RESULTS AND DISCUSSION

### A. Geometric properties and structural stability

Figure 1 shows the studied  $Y\text{-CrXTe}_3$  heterostructure, which is comprised of a  $\sqrt{3} \times \sqrt{3}$   $Y$  monolayer on top of which a  $1 \times 1$   $\text{CrXTe}_3$  monolayer is added. To neglect the influence of strain on magnetic properties of  $\text{CrXTe}_3$ , we use here the experimental in-plane lattice constants of  $\text{CrXTe}_3$  [44,45] for both the  $\text{CrXTe}_3$  and  $Y$  monolayers—implying that the  $Y$  monolayer is slightly strained. We consider six high-symmetry stacking configurations (denoted as I–VI) for all heterostructures, and the most stable configurations (as shown in Fig. 1 and Fig. S1 [43]) are determined to be V and III for  $Y\text{-CrI}_3$  and  $Y\text{-CrXTe}_3$ , respectively. These configurations are those employed in subsequent calculations. The inversion symmetry is naturally broken in the heterostructures and thus one can expect a finite DMI between the Cr ions to arise.

### B. Spin model and magnetic parameters

To investigate the salient features of magnetism in our systems, we adopt the following spin Hamiltonian:

$$H = \frac{1}{2} \sum_{\langle i,j \rangle} J_{ij} \mathbf{S}_i \cdot \mathbf{S}_j + \frac{1}{2} \sum_{\langle i,j \rangle} \mathbf{D}_{ij} \cdot (\mathbf{S}_i \times \mathbf{S}_j) + \sum_i K (\mathbf{S}_i \cdot \hat{z})^2, \quad (1)$$

where  $J_{ij}$  denotes the Heisenberg exchange coupling and  $\mathbf{D}_{ij}$  is the vector characterizing the DMI interaction, both of them running over all first nearest-neighbor (NN) Cr pairs. The third term represents the magnetocrystalline anisotropy (MAE) that runs over all Cr sites. The coefficients of Eq. (1) are listed in Table I and are extracted from DFT calculations and the four-state energy mapping method (see the Supplemental Material (SM) for details [43]). For comparison, we also calculated the magnetic parameters for  $Y\text{-CrI}_3$ . As one can see from Table I, the Heisenberg exchange coupling  $J$ 's are always ferromagnetic for all heterostructures. We also find that all the heterostructures, except for Si-CrSiTe<sub>3</sub> and Si-CrGeTe<sub>3</sub>, favor out-of-plane anisotropy, as a consequence of an interplay between the single ion anisotropy and exchange anisotropy [46] [note that  $K$  in Eq. (1) quantifies the total anisotropy, which is the sum of single ion and exchange

TABLE I. Magnetic parameters of the eight studied heterostructures.  $J$ ,  $D$ ,  $K$ ,  $K_{\text{sia}}$ , and  $K_{\text{exch}}$  represent the coefficient of exchange interaction, DMI, total MAE, single ion anisotropy, and exchange anisotropy, respectively. The negative (positive)  $K$  represents the easy-axis (easy-plane) anisotropy. Note that  $S = 3/2$  is used when extracting the magnetic parameters. The units of energy are meV.

	$J$	$D$	$ D/J $	$K$	$K_{\text{sia}}$	$K_{\text{exch}}$
Ge-CrI <sub>3</sub>	-5.794	0.454	0.078	-0.863	0.349	-1.558
Ge-CrSiTe <sub>3</sub>	-8.583	0.797	0.093	-0.031	0.441	-0.920
Ge-CrGeTe <sub>3</sub>	-8.681	0.857	0.098	-0.204	0.492	-1.191
Ge-CrSnTe <sub>3</sub>	-7.964	1.442	0.181	-0.542	0.788	-2.135
Si-CrI <sub>3</sub>	-5.653	0.462	0.082	-0.766	0.288	-1.338
Si-CrSiTe <sub>3</sub>	-8.348	0.973	0.117	0.091	0.536	-0.973
Si-CrGeTe <sub>3</sub>	-8.580	1.165	0.136	0.389	0.743	-1.096
Si-CrSnTe <sub>3</sub>	-8.521	1.632	0.192	-0.820	0.455	-1.735

anisotropy]—which is an important factor that can affect the formation of magnetic topological states.

We then turn to the DMI. As we mentioned above, DMI requires two ingredients: (i) SOC, and (ii) symmetry breaking. The first aspect is easily satisfied in our system due to the large SOC of ligand atom I/Te, which is responsible for DMI of 2D magnets [20–24,47,48]. However, although structural asymmetry exists in all heterostructures,  $Y$ -CrI<sub>3</sub> exhibits the smallest DMI compared to others, as shown in Table I. This is due to the weak vdW coupling between CrI<sub>3</sub> and germanene/silicene (the layer spacing of 3.22/3.33 Å reveals a typical vdW equilibrium space). Consequently, the structure of CrI<sub>3</sub> is barely changed (for instance, the bond length difference  $\Delta$  between the Cr-I bond close to and away from the interface is 0.018/0.015 Å for  $Y$ -CrI<sub>3</sub>, while the  $\Delta$  of the pristine CrI<sub>3</sub> is 0, as listed in Table II). Therefore, the weak extent of broken inversion symmetry leads to small DMI. For the  $Y$ -CrXTe<sub>3</sub> series, the covalent  $Y$ -X and  $Y$ -Te bonding nature is apparent, as shown in Fig. 2. Such strong interfacial coupling greatly distorts the structure of CrXTe<sub>3</sub> with a relatively large  $\Delta$  for the Cr-Te bond of 0.055–0.063 Å (note that the  $\Delta$  of the pristine CrXTe<sub>3</sub> is also 0) as compared with the aforementioned one of  $Y$ -CrI<sub>3</sub>. Furthermore, the charge redistribution in  $Y$ -CrXTe<sub>3</sub> can induce a built-in electric field, which points from the Te atom close to the interface to the one away from the interface, as illustrated in Fig. 2. In con-

TABLE II. The bond length (Å) of bonds  $A$  and  $B$  as depicted in Fig. 1, the bond length difference  $\Delta$  (Å) of bonds  $A$  and  $B$ , and charge transfer  $\Delta\rho$ . Note that the positive value of  $\Delta\rho$  means a charge flow from silicene/germanene to CrXTe<sub>3</sub>/CrI<sub>3</sub>.

	Bond A	Bond B	$\Delta$	$\Delta\rho$
Ge-CrI <sub>3</sub>	2.747	2.765	0.018	0.115
Ge-CrSiTe <sub>3</sub>	2.758	2.701	0.057	0.173
Ge-CrGeTe <sub>3</sub>	2.761	2.703	0.058	0.229
Ge-CrSnTe <sub>3</sub>	2.782	2.726	0.056	0.170
Si-CrI <sub>3</sub>	2.748	2.763	0.015	0.125
Si-CrSiTe <sub>3</sub>	2.756	2.701	0.055	0.325
Si-CrGeTe <sub>3</sub>	2.758	2.703	0.055	0.328
Si-CrSnTe <sub>3</sub>	2.720	2.783	0.063	0.197

trast,  $Y$ -CrI<sub>3</sub> has a negligible built-in electric field, even if there is charge transfer between CrI<sub>3</sub> and  $Y$  layer (as listed in Table II). Thus, the strong extent of broken inversion symmetry in  $Y$ -CrXTe<sub>3</sub> causes large DMIs. For the  $Y$ -CrXTe<sub>3</sub> series, the observed trend of  $D_{\text{CrSiTe}_3} < D_{\text{CrGeTe}_3} < D_{\text{CrSnTe}_3}$  correlates well with the increasing order of SOC of the  $X$  atom [Si( $\sim 10^{-3}$ ) < Ge( $\sim 10^{-2}$ ) < Sn( $\sim 10^{-1}$ )] [49,50]. We also note that the DMI coefficient of the Si-CrXTe<sub>3</sub> series is larger than that of the Ge-CrXTe<sub>3</sub> series, which could be explained from the larger charge transfer between CrXTe<sub>3</sub> and Si layer than between CrXTe<sub>3</sub> and Ge layer (as listed in Table II). Notably, the significant DMI/exchange ratios  $|D/J|$  of  $Y$ -CrXTe<sub>3</sub> demonstrate that the strong coupling heterostructure is an effective way to induce considerable DMI and is thus promising to create magnetic skyrmions.

### C. Curie temperature and ground state without external magnetic field

After we obtained all the parameters in the spin Hamiltonian of Eq. (1), parallel tempering Monte Carlo (PTMC) simulations are then performed over a  $60 \times 60 \times 1$  supercell to determine low-energy phases (see the SM for details). The initial spin textures are obtained from a full relaxation of the paramagnetic (random) state. We first extract the Curie temperature  $T_C$  of all the heterostructures by looking at the specific heat versus temperature. The  $T_C$  is 45 K for pristine monolayer CrI<sub>3</sub>, 43 K for CrSiTe<sub>3</sub>, 60 K for CrGeTe<sub>3</sub>, and 70 K for CrSnTe<sub>3</sub> [51]. As compared with free-standing single-layer CrI<sub>3</sub> and CrXTe<sub>3</sub>, all the heterostructures have increased  $T_C$ , as shown in Fig. 3, which is consistent with previous studies [52,53]. To guarantee the converged spin structures to be the ground state at the temperature of 0 K, the conjugate gradient (CG) method is further implemented to relax the spin textures obtained by PTMC simulations. Coupled with the large easy-axis anisotropy, the ground states of  $Y$ -CrI<sub>3</sub> are determined to be out-of-plane FM. There is also no sign of any chiral spin textures even with external magnetic field. These findings are consistent with the fact that the  $|D/J|$  ratios of  $Y$ -CrI<sub>3</sub> are found here to be 0.078 and 0.082, which falls outside the typical range 0.1–0.2 for the formation of skyrmions. We thus focus on the six  $Y$ -CrXTe<sub>3</sub> heterostructures in the following discussions.

Next, we first discuss the ground state of  $Y$ -CrXTe<sub>3</sub> heterostructures at 0 K without external magnetic field. As shown in Fig. 4, the  $Y$ -CrXTe<sub>3</sub> heterostructures with different  $|D/J|$  exhibit a distinct ground state. For Ge-CrSiTe<sub>3</sub>, Ge-CrGeTe<sub>3</sub>, and Si-CrSiTe<sub>3</sub>, parallel stripes phases are observed [see Figs. 4(a), 4(b), and 4(d)], which is a consequence of a similar  $|D/J|$  ratio 0.093–0.117. Specifically, the relatively larger  $|D/J|$  of Si-CrSiTe<sub>3</sub> results in narrower width stripes ( $\sim 20.2$  nm), compared with that of Ge-CrSiTe<sub>3</sub> and Ge-CrGeTe<sub>3</sub> ( $\sim 35.2$  and  $\sim 29.0$  nm)—as is consistent with Ref. [54]. On the other hand and due to a larger  $|D/J|$ , the ground states of Ge-CrSnTe<sub>3</sub>, Si-CrGeTe<sub>3</sub>, and Si-CrSnTe<sub>3</sub> all present labyrinth domain morphology but manifest different specific characteristics [as shown in Figs. 4(c), 4(e), and 4(f)]. For Si-CrGeTe<sub>3</sub>, the ground state consists of a connected labyrinth, which is in line with a lower  $|D/J|$  of 0.136 than that of Ge-CrSnTe<sub>3</sub> and Si-CrSnTe<sub>3</sub>, while for

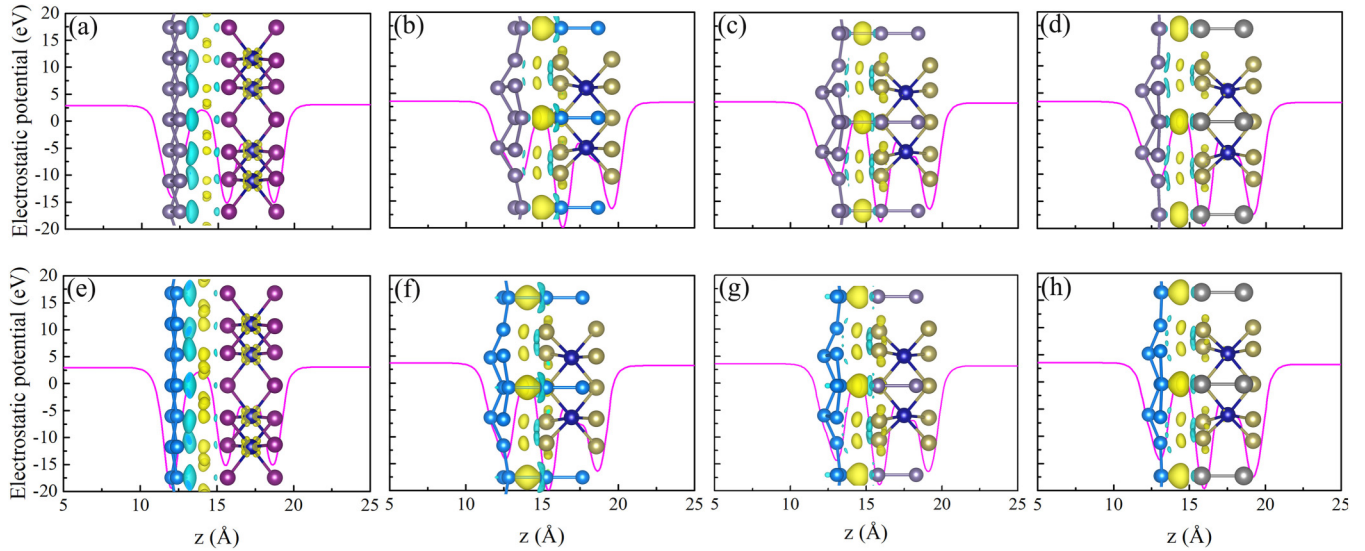


FIG. 2. Electrostatic potential and charge difference of (a) Ge-CrI<sub>3</sub>, (b) Ge-CrSiTe<sub>3</sub>, (c) Ge-CrGeTe<sub>3</sub>, (d) Ge-CrSnTe<sub>3</sub>, (e) Si-CrI<sub>3</sub>, (f) Si-CrSiTe<sub>3</sub>, (g) Si-CrGeTe<sub>3</sub>, (h) Si-CrSnTe<sub>3</sub>, respectively.

Ge-CrSnTe<sub>3</sub>, that has a  $|D/J|$  of 0.181, the ground state is made of disconnected labyrinths. Interestingly, an isolated skyrmion emerges on the background of the labyrinth domain in Si-CrSnTe<sub>3</sub>, which possesses the even higher  $|D/J|$  of 0.192.

#### D. Effects of magnetic field on topological spin textures

Let us now look into the effects of magnetic field on topological spin structures of  $Y$ -CrXTe<sub>3</sub> heterostructures at 0 K. To this end, we have derived from our simulations the field dependence of topological charge  $Q$  per supercell (see the SM for details, and Fig. 5). In conjunction with the real-space images of Fig. 4, the values of  $Q$  can help us identify

the different phases. For examples,  $Q = 0$  can correspond to stripes, labyrinths, or the FM state, while finite values of  $Q$  indicate the emergence of skyrmions. The external magnetic field is oriented outward from the  $Y$  layer. For the case of Ge-CrSiTe<sub>3</sub> and Ge-CrGeTe<sub>3</sub>, a phase, to be denoted as phase II and consisting of isolated skyrmions, begins to appear at about 0.1 T, as indicated in Figs. 5(a) and 5(b). The diameter of skyrmions decreases when the magnetic field increases. Above 0.5 T, the Ge-CrSiTe<sub>3</sub> adopts a uniform FM state, to be coined as phase VIII. Because of the relatively large easy-axis anisotropy, the Ge-CrGeTe<sub>3</sub> transforms into phase VIII above 0.4 T [55]. In contrast, for Si-CrSiTe<sub>3</sub>, we find a tendency evolving from parallel stripes (phase I) at low field,

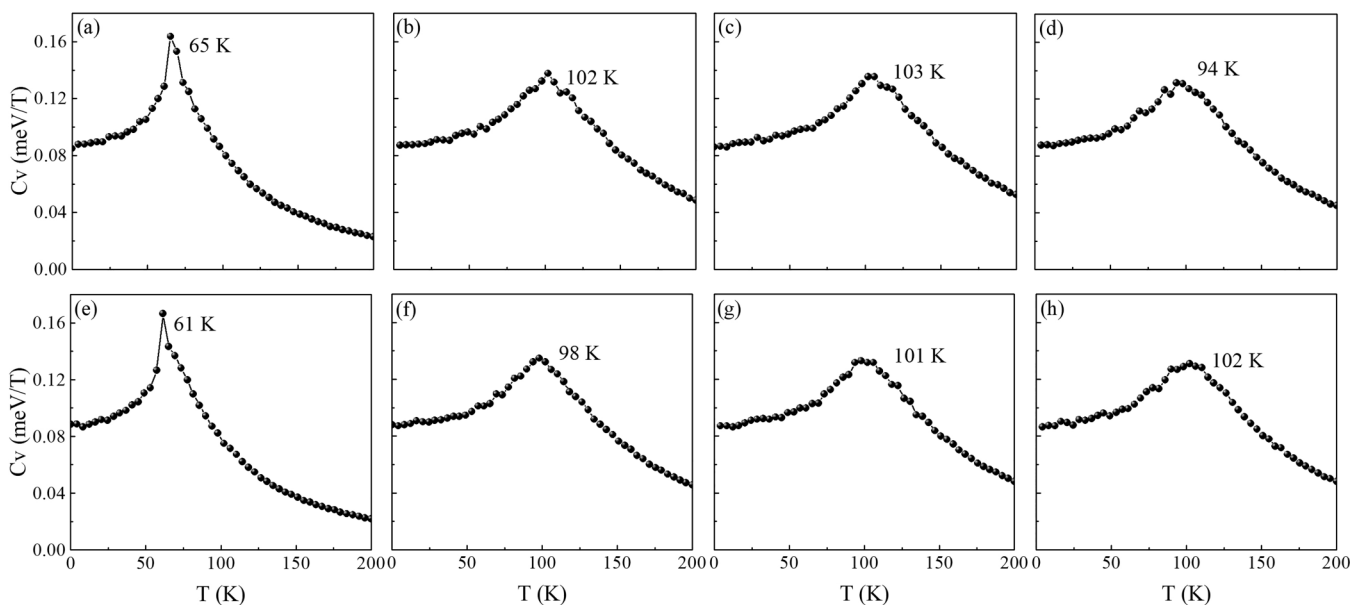


FIG. 3. The calculated specific heat of (a) Ge-CrI<sub>3</sub>, (b) Ge-CrSiTe<sub>3</sub>, (c) Ge-CrGeTe<sub>3</sub>, (d) Ge-CrSnTe<sub>3</sub>, (e) Si-CrI<sub>3</sub>, (f) Si-CrSiTe<sub>3</sub>, (g) Si-CrGeTe<sub>3</sub>, (h) Si-CrSnTe<sub>3</sub> as a function of temperature.

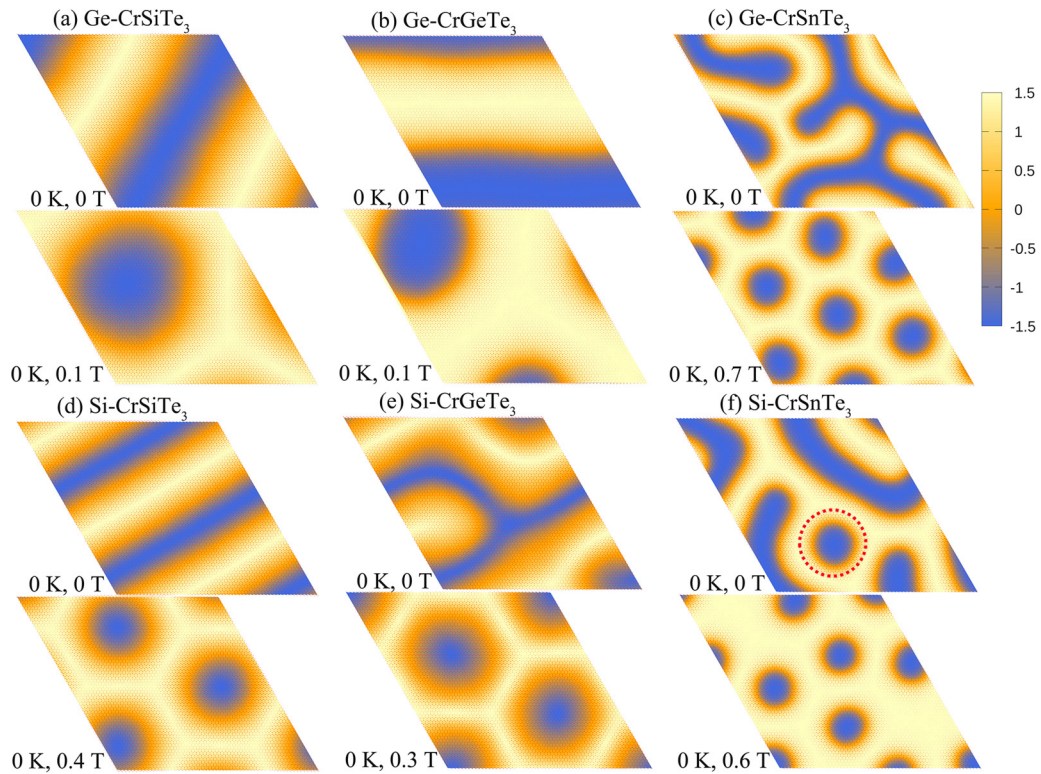


FIG. 4. Representative spin texture of (a) Ge-CrSiTe<sub>3</sub>, (b) Ge-CrGeTe<sub>3</sub>, (c) Ge-CrSnTe<sub>3</sub>, (d) Si-CrSiTe<sub>3</sub>, (e) Si-CrGeTe<sub>3</sub>, and (f) Si-CrSnTe<sub>3</sub> with and without applying magnetic field ( $B$ ) at 0 K. The skyrmion embedded in labyrinth domains for Si-CrSnTe<sub>3</sub> is highlighted with a red circle.

to a triangular skyrmion lattice (phase V) in the magnetic field range 0.1–1.0 T, as depicted in Fig. 5(d). One can attribute the emergence of the skyrmion lattice under field to the small value of the easy-plane MAE of Si-CrSiTe<sub>3</sub>, even though its

$|D/J|$  is of 0.117, which is close to the lower limit of the skyrmion existence range [32,55]. When the magnetic field further increases from 1.0 to 1.2 T, the size of skyrmion also decreases, along with the skyrmion density. Similarly, due

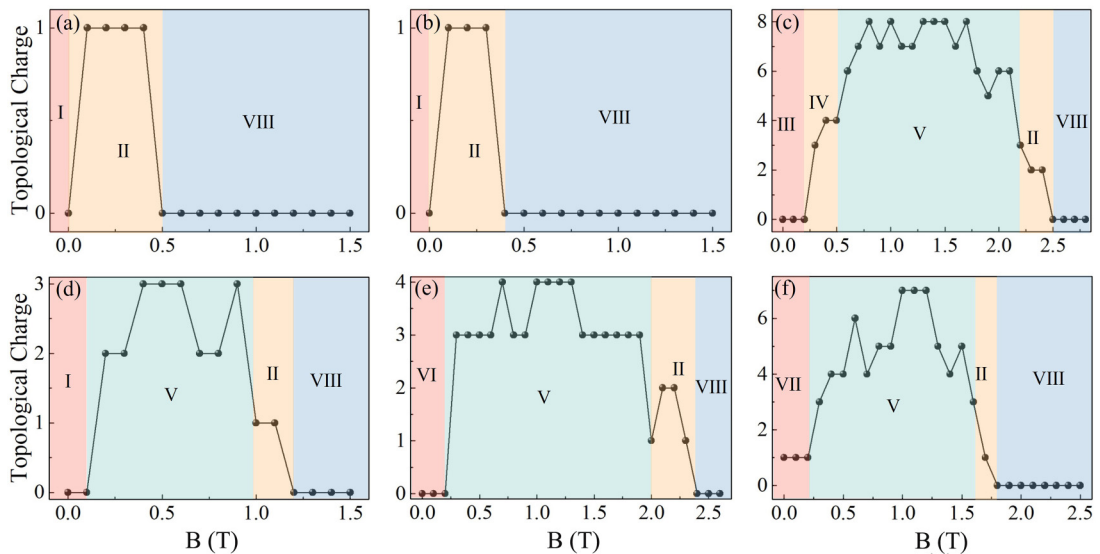


FIG. 5. The topological charge  $|Q|$  for (a) Ge-CrSiTe<sub>3</sub>, (b) Ge-CrGeTe<sub>3</sub>, (c) Ge-CrSnTe<sub>3</sub>, (d) Si-CrSiTe<sub>3</sub>, (e) Si-CrGeTe<sub>3</sub>, (f) Si-CrSnTe<sub>3</sub> as a function of  $B$  at 0 K. The eight phases found are as follows: parallel stripes (I), discrete skyrmion (II), disconnected labyrinths (III), fragmented (“wormlike”) labyrinth domains and skyrmion mixed phase (IV), skyrmion lattice (V), connected labyrinth (VI), disconnected labyrinths and skyrmion mixed phase (VII), and saturated ferromagnetic state (VIII), respectively.

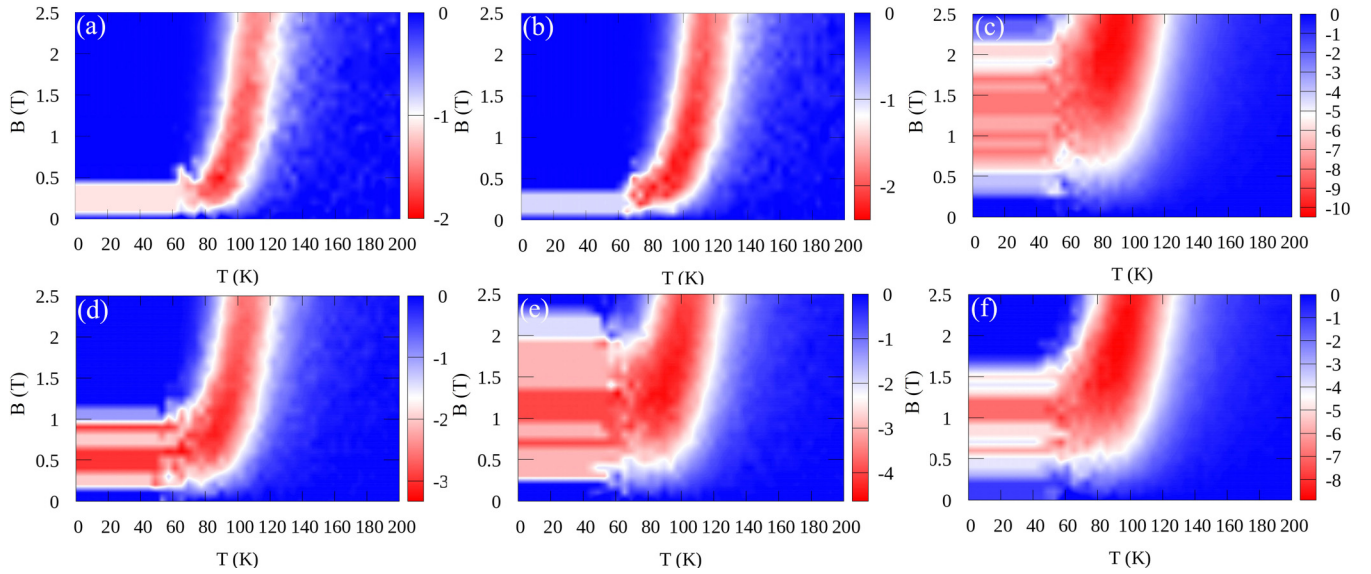


FIG. 6. The topological charge  $Q$  per supercell of (a) Ge-CrSiTe<sub>3</sub>, (b) Ge-CrGeTe<sub>3</sub>, (c) Ge-CrSnTe<sub>3</sub>, (d) Si-CrSiTe<sub>3</sub>, (e) Si-CrGeTe<sub>3</sub>, (f) Si-CrSnTe<sub>3</sub> as a function of temperature and external magnetic field  $B$ .

to the same reason of easy-plane anisotropy, we also find a robust skyrmion lattice phase in the magnetic range 0.2–2.0 T for Si-CrGeTe<sub>3</sub>, as displayed in Fig. 5(e). For the case of Ge-CrSnTe<sub>3</sub>, the magnetic field (0.2–0.5 T) first tends to break the disconnected labyrinth domain (phase III) into fragmental domains mixed with skyrmions [phase IV, as depicted in Fig. 5(c) and Fig. S2(c) of the SM [43]]. Further increments of magnetic field (0.5–2.2 T) totally wipe out the labyrinth states and the skyrmions now organize themselves into a triangular lattice which is representative of phase V. With respect to that of Ge-CrSnTe<sub>3</sub>, the skyrmion lattice phase of Si-CrSnTe<sub>3</sub> can be preserved in a relatively narrow magnetic field range 0.2–1.6 T [Fig. 5(f)] owing to the large easy-axis anisotropy. Moreover, Si-CrSnTe<sub>3</sub> is easier to magnetize and to transform into the FM state than Ge-CrSnTe<sub>3</sub> (the critical fields leading to FM are 1.8 and 2.5 T in these two compounds, respectively).

### E. Phase diagram ( $B$ - $T$ ) and thermal fluctuation effects on topology

Finally, we establish a magnetic field versus temperature phase diagram ( $B$ - $T$ ) for the topological charge  $Q$  per supercell, in order to gain more insight into the thermal destabilization of skyrmions. One can clearly see from Fig. 6 that, approximately below 70 K and in the same magnetic field range as that in Fig. 5, skyrmions or skyrmion lattice of  $Y$ -Cr $X$ Te<sub>3</sub> heterostructures can be well preserved. For a given  $B$ , the topological charge does not change much as the temperature is progressively increased up to 70 K. One should note that the image of the skyrmions begins to be blurred above about 70 K, as shown in Fig. 7(a). However, we notice that the value of  $Q$  is still significant along a ridge extending to the high temperature and large magnetic field

region, where no skyrmions are expected. As already discussed in a previous study [56], this emergence of such topological charge originates from thermal fluctuation. To illustrate the thermal fluctuation effects on topology, we take Si-CrSnTe<sub>3</sub> at  $B = 0.6$  T as a typical example. As discussed above, the topological charge is  $Q = -6$ . At the same field, if the temperature is elevated to point A (about 65 K), the snapshot in Fig. 7(a) presents blurred skyrmions with slightly decreased topological charge of  $-5.88$ , which originates from thermal activation effects. Although the topological charge ( $-3.64$ ) at point B (about 102 K) remains finite, the image shown in Fig. 7(b) is completely random. When we move to the high-field and high-temperature point C (2.0 T, 102 K), where no skyrmion is expected, the topological charge ( $-8.48$ ) is however still significant. The image shown in

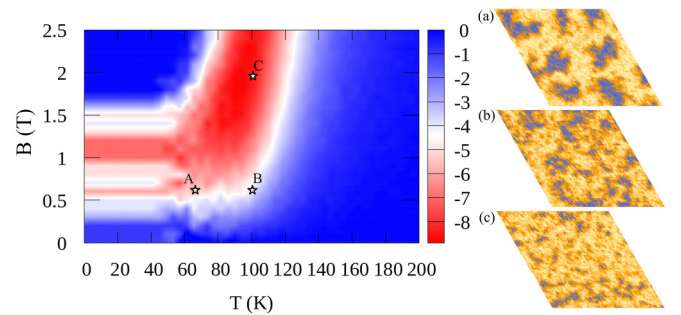


FIG. 7. The phase diagram of topological charges for Si-CrSnTe<sub>3</sub> with the magnetic field and temperature dependence. Star symbols labeled A to C correspond to the snapshots in panels (a)–(c).

Fig. 7(c) again depicts uniform randomness and the absence of any spin ordering at this point.

#### IV. SUMMARY

In summary, using first-principle calculations and MC simulations, we discovered that  $Y\text{-CrXTe}_3$  heterostructures represent a different materials' family hosting skyrmions. Such latter topological defects result from interfacial engineering, which is known to induce DMI and stabilize novel spin textures in other compounds [26–30]. Moreover, recent experimental studies have shown that germanene/silicene can be grown on the  $\text{MoS}_2$  substrate [57–59], suggesting that a similar epitaxial growth scheme might be extended to other 2D magnetic insulating substrates such as  $\text{CrSiTe}_3$  or  $\text{CrGeTe}_3$ . The required SOC and inversion asymmetry are both intrinsic properties of our heterostructure system, thus leading to inherent large DMI, which can be roughly measured by the extent of inversion symmetry breaking. We also find that skyrmions (skyrmion lattices) can be stabilized over a relatively wide range of magnetic fields and temperatures. Therefore, we hope that our work has

important implications to, e.g., design 2D skyrmion-based logic and memory devices.

#### ACKNOWLEDGMENTS

This work was supported by the National Natural Science Foundation of China (Grant No. 11704007), Natural Science Basic Research Plan in Shaanxi Province of China (Grants No. 2022JQ-008 and No. 2022JM-035), Open Foundation of Key Laboratory of Computational Physical Sciences (Ministry of Education), and Open Foundation of State Key Laboratory of Surface Physics and Department of Physics (Grant No. KF2022\_14). L.B. acknowledges Vannevar Bush Faculty Fellowship Grant No. N00014-20-1-2834 from the Department of Defense. H.Z. and X.X. were supported by National Natural Science Foundation of China (Grants No. 12274276 and No. 12174237). Calculations were performed at the High-Performance Computing Center of Baoji University of Arts and Sciences and partly at the High-Performance Computing Center of Hunan Institute of Advanced Sensing and Information Technology in Xiangtan University.

- 
- [1] S. Mühlbauer, B. Binz, F. Jonietz, C. Pfleiderer, A. Rosch, A. Neubauer, R. Georgii, and P. Boni, Skyrmion lattice in a chiral magnet, *Science* **323**, 915 (2009).
- [2] N. Nagaosa and Y. Tokura, Topological properties and dynamics of magnetic skyrmions, *Nat. Nanotechnol.* **8**, 899 (2013).
- [3] A. Fert, N. Reyren, and V. Cros, Magnetic skyrmions: advances in physics and potential applications, *Nat. Rev. Mater.* **2**, 17031 (2017).
- [4] S. Parkin and S. H. Yang, Memory on the racetrack, *Nat. Nanotechnol.* **10**, 195 (2015).
- [5] I. Dzyaloshinsky, A thermodynamic theory of “weak” ferromagnetism of antiferromagnetics, *J. Phys. Chem. Solids* **4**, 241 (1958).
- [6] T. Moriya, Anisotropic superexchange interaction and weak ferromagnetism, *Phys. Rev.* **120**, 91 (1960).
- [7] A. K. Srivastava, P. Devi, A. K. Sharma, T. P. Ma, H. Deniz, H. L. Meyerheim, C. Felser, and S. S. P. Parkin, Observation of robust Néel skyrmions in metallic  $\text{PtMnGa}$ , *Adv. Mater.* **32**, 1904327 (2020).
- [8] A. K. Nayak, V. Kumar, T. P. Ma, P. Werner, E. Pippel, R. Sahoo, F. Damay, U. K. Röbber, C. Felser, and S. S. P. Parkin, Magnetic antiskyrmions above room temperature in tetragonal Heusler materials, *Nature (London)* **548**, 561 (2017).
- [9] X. Z. Yu, N. Kanazawa, Y. Onose, K. Kimoto, W. Z. Zhang, S. Ishiwata, Y. Matsui, and Y. Tokura, Near room-temperature formation of a skyrmion crystal in thin-films of the helimagnet  $\text{FeGe}$ , *Nat. Mater.* **10**, 106 (2011).
- [10] I. Kézsmárki, S. Bordács, P. Milde, E. Neuber, L. M. Eng, J. S. White, H. M. Rønnow, C. D. Dewhurst, M. Mochizuki, K. Yanai, H. Nakamura, D. Ehlers, V. Tsurkan, and A. Loidl, Néel-type skyrmion lattice with confined orientation in the polar magnetic semiconductor  $\text{GaV}_4\text{S}_8$ , *Nat. Mater.* **14**, 1116 (2015).
- [11] S. Heinze, K. Bergmann, M. Menzel, J. Brede, A. Kubetzka, R. Wiesendanger, G. Bihlmayer, and S. Blügel, Spontaneous atomic-scale magnetic skyrmion lattice in two dimensions, *Nat. Phys.* **7**, 713 (2011).
- [12] S. D. Pollard, J. A. Garlow, J. W. Yu, Z. Wang, Y. M. Zhu, and H. Yang, Observation of stable Néel skyrmions in cobalt/palladium multilayers with Lorentz transmission electron microscopy, *Nat. Commun.* **8**, 14761 (2017).
- [13] O. Boulle, J. Vogel, H. X. Yang, S. Pizzini, D. S. Chaves, A. Locatelli, T. O. Menteş, A. Sala, L. D. Buda-Prejbeanu, O. Klein, M. Belmeguenai, Y. Roussigné, A. Stashkevich, S. M. Chérif, L. Aballe, M. Foerster, M. Chshiev, S. Auffret, I. M. Miron, and G. Gaudin, Room-temperature chiral magnetic skyrmions in ultrathin magnetic nanostructures, *Nat. Nanotechnol.* **11**, 449 (2016).
- [14] S. Woo, K. Litzius, B. Krüger, M. Y. Im, L. Caretta, K. Richter, M. Mann, A. Krone, R. M. Reeve, M. Weigand, P. Agrawal, I. Lemesch, M. A. Mawass, P. Fischer, M. Kläui, and G. S. D. Beach, Observation of room-temperature magnetic skyrmions and their current-driven dynamics in ultrathin metallic ferromagnets, *Nat. Mater.* **15**, 501 (2016).
- [15] C. Moreau-Luchaire, C. Moutafis, N. Reyren, J. Sampaio, C. A. F. Vaz, N. Van Horne, K. Bouzehouane, K. Garcia, C. Deranlot, P. Warnicke, P. Wohlhüter, J.-M. George, M. Weigand, J. Raabe, V. Cros, and A. Fert, Additive interfacial chiral interaction in multilayers for stabilization of small individual skyrmions at room temperature, *Nat. Nanotechnol.* **11**, 444 (2016).
- [16] C. Gong, L. Li, Z. L. Li, H. W. Ji, A. Stern, Y. Xia, T. Cao, W. Bao, C. Z. Wang, Y. Wang, Z. Q. Qiu, R. J. Cava, S. G. Louie, J. Xia, and X. Zhang, Discovery of intrinsic ferromagnetism in two-dimensional van der Waals crystals, *Nature (London)* **546**, 265 (2017).
- [17] B. Huang, G. Clark, E. Navarro-Moratalla, D. R. Klein, R. Cheng, K. L. Seyler, D. Zhong, E. Schmidgall, M. A. McGuire, D. H. Cobden, W. Yao, D. Xiao, P. Jarillo-Herrero, and X. D. Xu, Layer-dependent ferromagnetism in a van der Waals

- crystal down to the monolayer limit, *Nature (London)* **546**, 270 (2017).
- [18] B. J. Liu, Y. M. Zou, L. Zhang, S. M. Zhou, Z. Wang, W. K. Wang, Z. Qu, and Y. H. Zhang, Critical behavior of the quasi-two-dimensional semiconducting ferromagnet CrSiTe<sub>3</sub>, *Sci. Rep.* **6**, 33873 (2016).
- [19] M. W. Lin, H. L. Zhuang, J. Yan, T. Z. Ward, A. A. Puretzy, C. M. Rouleau, Z. Gai, L. Liang, V. Meunier, B. G. Sumpter, P. Ganesh, P. R. C. Kent, D. B. Geohegan, D. G. Mandrus, and K. Xiao, Ultrathin nanosheets of CrSiTe<sub>3</sub>: A semiconducting two-dimensional ferromagnetic material, *J. Mater. Chem. C* **4**, 315 (2016).
- [20] J. Liang, W. Wang, H. Du, A. Hallal, K. Garcia, M. Chshiev, A. Fert, and H. Yang, Very large Dzyaloshinskii-Moriya interaction in two-dimensional Janus manganese dichalcogenides and its application to realize skyrmion states, *Phys. Rev. B* **101**, 184401 (2020).
- [21] J. Yuan, Y. Yang, Y. Cai, Y. Wu, Y. Chen, X. Yan, and L. Shen, Intrinsic skyrmions in monolayer Janus magnets, *Phys. Rev. B* **101**, 094420 (2020).
- [22] C. Xu, J. Feng, S. Prokhorenko, Y. Nahas, H. Xiang, and L. Bellaïche, Topological spin texture in Janus monolayers of the chromium trihalides Cr(I, X)<sub>3</sub>, *Phys. Rev. B* **101**, 060404(R) (2020).
- [23] Y. Zhang, C. Xu, P. Chen, Y. Nahas, S. Prokhorenko, and L. Bellaïche, Emergence of skyrmionium in a two-dimensional CrGe(Se, Te)<sub>3</sub> Janus monolayer, *Phys. Rev. B* **102**, 241107(R) (2020).
- [24] Q. Cui, J. Liang, Z. Shao, P. Cui, and H. Yang, Strain-tunable ferromagnetism and chiral spin textures in two-dimensional Janus chromium dichalcogenides, *Phys. Rev. B* **102**, 094425 (2020).
- [25] J. Liu, M. Shi, J. Lu, and M. P. Anantram, Analysis of electrical-field-dependent Dzyaloshinskii-Moriya interaction and magnetocrystalline anisotropy in a two-dimensional ferromagnetic monolayer, *Phys. Rev. B* **97**, 054416 (2018).
- [26] Y. Wu, S. Zhang, J. Zhang, W. Wang, Y. L. Zhu, J. Hu, G. Yin, K. Wong, C. Fang, C. Wan, X. Han, Q. Shao, T. Taniguchi, K. Watanabe, J. Zang, Z. Mao, X. Zhang, and K. L. Wang, Néel-type skyrmion in WTe<sub>2</sub>/Fe<sub>3</sub>GeTe<sub>2</sub> van der Waals heterostructure, *Nat. Commun.* **11**, 3860 (2020).
- [27] W. Sun, W. Wang, H. Li, G. Zhang, D. Chen, J. Wang, and Z. Cheng, Controlling bimerons as skyrmion analogues by ferroelectric polarization in 2D van der Waals multiferroic heterostructures, *Nat. Commun.* **11**, 5930 (2020).
- [28] W. Sun, W. Wang, J. Zang, H. Li, G. Zhang, J. Wang, and Z. Cheng, Manipulation of magnetic skyrmion in a 2D van der Waals heterostructure via both electric and magnetic fields, *Adv. Funct. Mater.* **31**, 2104452 (2021).
- [29] C. K. Li, X. P. Yao, and G. Chen, Writing and deleting skyrmions with electric fields in a multiferroic heterostructure, *Phys. Rev. Res.* **3**, L012026 (2021).
- [30] S. Fragkos, P. Pappas, E. Symeonidou, Y. Panayiotatos, and A. Dimoulas, Magnetic skyrmion manipulation in CrTe<sub>2</sub>/WTe<sub>2</sub> 2D van der Waals heterostructure, *Appl. Phys. Lett.* **120**, 182402 (2022).
- [31] D. Z. Li, S. Haldar, and S. Heinze, Strain-Driven Zero-Field Near-10 nm Skyrmions in Two-Dimensional van der Waals Heterostructures, *Nano Lett.* **22**, 7706 (2022).
- [32] A. Fert, V. Cros, and J. Sampaio, Skyrmions on the track, *Nat. Nanotechnol.* **8**, 152 (2013).
- [33] G. Kresse and J. Furthmüller, Efficient iterative schemes for ab initio total-energy calculations using a plane-wave basis set, *Phys. Rev. B* **54**, 11169 (1996).
- [34] G. Kresse and J. Hafner, Ab initio molecular dynamics for liquid metals, *Phys. Rev. B* **47**, 558 (1993).
- [35] J. P. Perdew, K. Burke, and M. Ernzerhof, Generalized Gradient Approximation Made Simple, *Phys. Rev. Lett.* **77**, 3865 (1996).
- [36] S. Grimme, Semiempirical GGA-type density functional constructed with a long-range dispersion correction, *J. Comput. Chem.* **27**, 1787 (2006).
- [37] H. J. Xiang, E. J. Kan, S. H. Wei, M. H. Whangbo, and X. G. Gong, Predicting the spin-lattice order of frustrated systems from first principles, *Phys. Rev. B* **84**, 224429 (2011).
- [38] G. Menichetti, M. Calandra, and M. Polini, Electronic structure and magnetic properties of few-layer Cr<sub>2</sub>Ge<sub>2</sub>Te<sub>6</sub>: The key role of nonlocal electron-electron interaction effects, *2D Mater.* **6**, 045042 (2019).
- [39] H. Xiang, C. Lee, H. J. Koo, X. Gong, and M. H. Whangbo, Magnetic properties and energy-mapping analysis, *Dalton Trans.* **42**, 823 (2013).
- [40] C. Xu, B. Xu, B. Dupé, and L. Bellaïche, Magnetic interactions in BiFeO<sub>3</sub>: A first-principles study, *Phys. Rev. B* **99**, 104420 (2019).
- [41] H. J. Xiang, S. H. Wei, and M. H. Whangbo, Origin of the Structural and Magnetic Anomalies of the Layered Compound SrFeO<sub>2</sub>: A Density Functional Investigation, *Phys. Rev. Lett.* **100**, 167207 (2008).
- [42] P. S. Wang and H. J. Xiang, Room-temperature Ferrimagnet with Frustrated Antiferroelectricity: Promising Candidate Toward Multiple-State Memory, *Phys. Rev. X* **4**, 011035 (2014).
- [43] See Supplemental Material at <http://link.aps.org/supplemental/10.1103/PhysRevB.107.024402> for detailed methods and further discussion on our results, which includes Refs. [41,42,52,53,60–64].
- [44] Y. Liu and C. Petrovic, Anisotropic magnetic entropy change in Cr<sub>2</sub>X<sub>2</sub>Te<sub>6</sub> (X = Si and Ge), *Phys. Rev. Mater.* **3**, 014001 (2019).
- [45] H. L. Zhuang, Y. Xie, P. R. C. Kent, and P. Ganesh, Computational discovery of ferromagnetic semiconducting single-layer CrSnTe<sub>3</sub>, *Phys. Rev. B* **92**, 035407 (2015).
- [46] J. L. Lado and J. Fernández-Rossier, On the origin of magnetic anisotropy in two dimensional CrI<sub>3</sub>, *2D Mater.* **4**, 035002 (2017).
- [47] Q. Cui, Y. Zhu, Y. Ga, J. Liang, P. Li, D. Yu, P. Cui, and H. Yang, Anisotropic dzyaloshinskii-moriya interaction and topological magnetism in two-dimensional magnets protected by P4m2 crystal symmetry, *Nano Lett.* **22**, 2334 (2022).
- [48] W. Du, K. Dou, Z. He, Y. Dai, B. Huang, and Y. Ma, Spontaneous magnetic skyrmions in single-layer CrInX<sub>3</sub> (X = Te, Se), *Nano Lett.* **22**, 3440 (2022).
- [49] M. Blume and R. E. Watson, Theory of spin-orbit coupling in atoms, II. Comparison of theory with experiment, *Proc. Math. Phys. Eng. Sci.* **271**, 565 (1963).
- [50] W. C. Martin, Table of spin-orbit energies for p-electrons in neutral atomic (core) np configurations, *J. Res. Natl. Bur. Stand., Sect. A* **75**, 109 (1971).
- [51] B. L. Chittari, D. Lee, N. Banerjee, A. H. MacDonald, E. Hwang, and J. Jung, Carrier- and strain-tunable intrinsic



- magnetism in two-dimensional MAX<sub>3</sub> transition metal chalcogenides, *Phys. Rev. B* **101**, 085415 (2020).
- [52] H. Li, Y. K. Xu, K. Lai, and W. B. Zhang, The enhanced ferromagnetism of single-layer CrX<sub>3</sub> (X = Br and I) via van der Waals engineering, *Phys. Chem. Chem. Phys.* **21**, 11949 (2019).
- [53] H. Zhang, W. Qin, M. Chen, P. Cui, Z. Zhang, and X. Xu, Converting a two-dimensional ferromagnetic insulator into a high-temperature quantum anomalous Hall system by means of an appropriate surface modification, *Phys. Rev. B* **99**, 165410 (2019).
- [54] I. Lemesch, F. Büttner, and G. S. Beach, Accurate model of the stripe domain phase of perpendicularly magnetized multilayers, *Phys. Rev. B* **95**, 174423 (2017).
- [55] S. Banerjee, J. Rowland, O. Erten, and M. Randeria, Enhanced Stability of Skyrmions in Two-Dimensional Chiral Magnets with Rashba Spin-Orbit Coupling, *Phys. Rev. X* **4**, 031045 (2014).
- [56] W. T. Hou, J. X. Yu, M. Daly, and J. Zang, Thermally driven topology in chiral magnets, *Phys. Rev. B* **96**, 140403(R) (2017).
- [57] L. Zhang, P. Bampoulis, A. N. Rudenko, Q. Yao, A. van Houselt, B. Poelsema, M. I. Katsnelson, and H. J. W. Zandvliet, Structural and Electronic Properties of Germanene on MoS<sub>2</sub>, *Phys. Rev. Lett.* **116**, 256804 (2016).
- [58] Z. Jiao, Q. Yao, A. N. Rudenko, L. Zhang, and H. J. W. Zandvliet, Germanium/MoS<sub>2</sub>: Competition between the growth of germanene and intercalation, *Phys. Rev. B* **102**, 205419 (2020).
- [59] A. Molle, A. Lamperti, D. Rotta, M. Fanciulli, E. Cinquanta, and C. Grazianetti, Electron confinement at the Si/MoS<sub>2</sub> heterosheet interface, *Adv. Mater. Interfaces* **3**, 1500619 (2016).
- [60] Y. Miyatake, M. Yamamoto, J. J. Kim, M. Toyonaga, and O. Nagai, On the implementation of the 'heat bath' algorithms for Monte Carlo simulations of classical Heisenberg spin systems, *J. Phys. C* **19**, 2539 (1986).
- [61] M. R. Hestenes and E. Stiefel, Methods of conjugate gradients for solving linear systems, *J. Res. Natl. Bur. Stand.* **49**, 409 (1952).
- [62] B. Berg and M. Lüscher, Definition and statistical distributions of a topological number in the lattice O(3)  $\sigma$ -model, *Nucl. Phys. B* **190**, 412 (1981).
- [63] G. Henkelman, A. Arnaldsson, and H. Jónsson, A fast and robust algorithm for Bader decomposition of charge density, *Comput. Mater. Sci.* **36**, 354 (2006).
- [64] M. X. Chen, Z. Zhong, and M. Weinert, Designing substrates for silicene and germanene: First-principles calculations, *Phys. Rev. B* **94**, 075409 (2016).